Shallow Subsurface Structure in the Hualien Basin and Relevance to the Damage Pattern and Fault Rupture during the 2018 Hualien Earthquake

Masumi Yamada[*1], Ikuo Cho[2], Chun-Hsiang Kuo[3], Che-Min Lin[4], Ken Miyakoshi[5], Yujia Guo[5], Takumi Hayashida[6], Yasuhiro Matsumoto[7], Jim Mori[1], Yin-Tung Yen[8], and Keng-Chang Kuo[9]

ABSTRACT

The 2018 M_w 6.4 Hualien earthquake generated a large peak-to-peak velocity of over 2 m/s, with a period of 3 s at the south end of the Milun fault, which resulted in the collapse of five buildings. To investigate the shallow subsurface soil structure and evaluate possible effects on the ground motion and building damage, we performed microtremor measurements in the Hualien basin. Based on the velocity structure jointly inverted from both Rayleigh-wave dispersion curves and microtremor horizontal-to-vertical spectral ratio data, we found that the shallow subsurface structure generally deepens from west to east. Close to the Milun fault, the structure becomes shallower, which is consistent with faulting during the 2018 earthquake and the long-term tectonic displacement. There is no significant variation for the site conditions in the north–south direction that can explain the large peak ground velocity in the south. As a result of the dense measurements in the heavily damaged area, where three high-rise buildings totally collapsed, these locations have the average *S*-wave velocity of the upper 30 m (AV_{S30}) values and are relatively high compared to the more distant area from the Meilun River. This is somewhat unusual, because lower AV_{S30} values indicating softer ground conditions are expected close to the river. We did not find any characteristic subsurface soil structure that may contribute to the building collapses. The large 3 s pulse was probably generated by source effects, rather than subsurface soil amplification.

KEY POINTS

- We performed microtremor measurements in the Hualien basin to investigate the shallow subsurface structure.
- We found that the change of subsurface soil structure caused by the faulting due to the tectonic structure.
- The large pulse during the mainshock was generated by source effects, rather than subsurface amplification.

Supplemental Material

INTRODUCTION

The 6 February 2018 M_w 6.4 Hualien, Taiwan, earthquake (at 23:50:43 local time) showed a very complex fault structure. The moment tensor mechanism shows a substantial non-double-couple component (e.g., U.S. Geological Survey website, see Data and Resources), which suggests there were multiple fault geometries. The source models in the seismic waveform and geodetic inversions (e.g., Huang and Huang, 2018; Lee *et al.*, 2019; Lo *et al.*, 2019) use multiple fault planes to explain the observed data.

The Milun fault, one of the fault structures causing the earthquake, runs in a north–south direction through the center of the Hualien basin (Fig. 1). This fault previously ruptured on 22 October 1951, causing an M_L 7.1–7.3 earthquake (Lo *et al.*, 2012). At that time, surface rupture appeared in downtown

1. Disaster Prevention Research Institute, Kyoto University, Uji, Japan; 2. National Institute of Advanced Industrial Science and Technology, Tsukuba, Japan; 3. National Central University, Taoyuan, Taiwan; 4. National Center for Research on Earthquake Engineering, Taipei, Taiwan; 5. Geo-Research Institute, Osaka, Japan; 6. Building Research Institute, Tsukuba, Japan; 7. Kozo Keikaku Engineering Inc., Tokyo, Japan; 8. Sinotech Engineering Consultants, Inc., Taipei, Taiwan; 9. Kaohsiung University of Science and Technology, Kaohsiung, Taiwan

*Corresponding author: masumi@eqh.dpri.kyoto-u.ac.jp

Cite this article as Yamada, M., I. Cho, C.-H. Kuo, C.-M. Lin, K. Miyakoshi, Y. Guo, T. Hayashida, Y. Matsumoto, J. Mori, Y.-T. Yen, *et al.* (2020). Shallow Subsurface Structure in the Hualien Basin and Relevance to the Damage Pattern and Fault Rupture during the 2018 Hualien Earthquake, *Bull. Seismol. Soc. Am.* **110**, 2939–2952, doi: 10.1785/0120200063

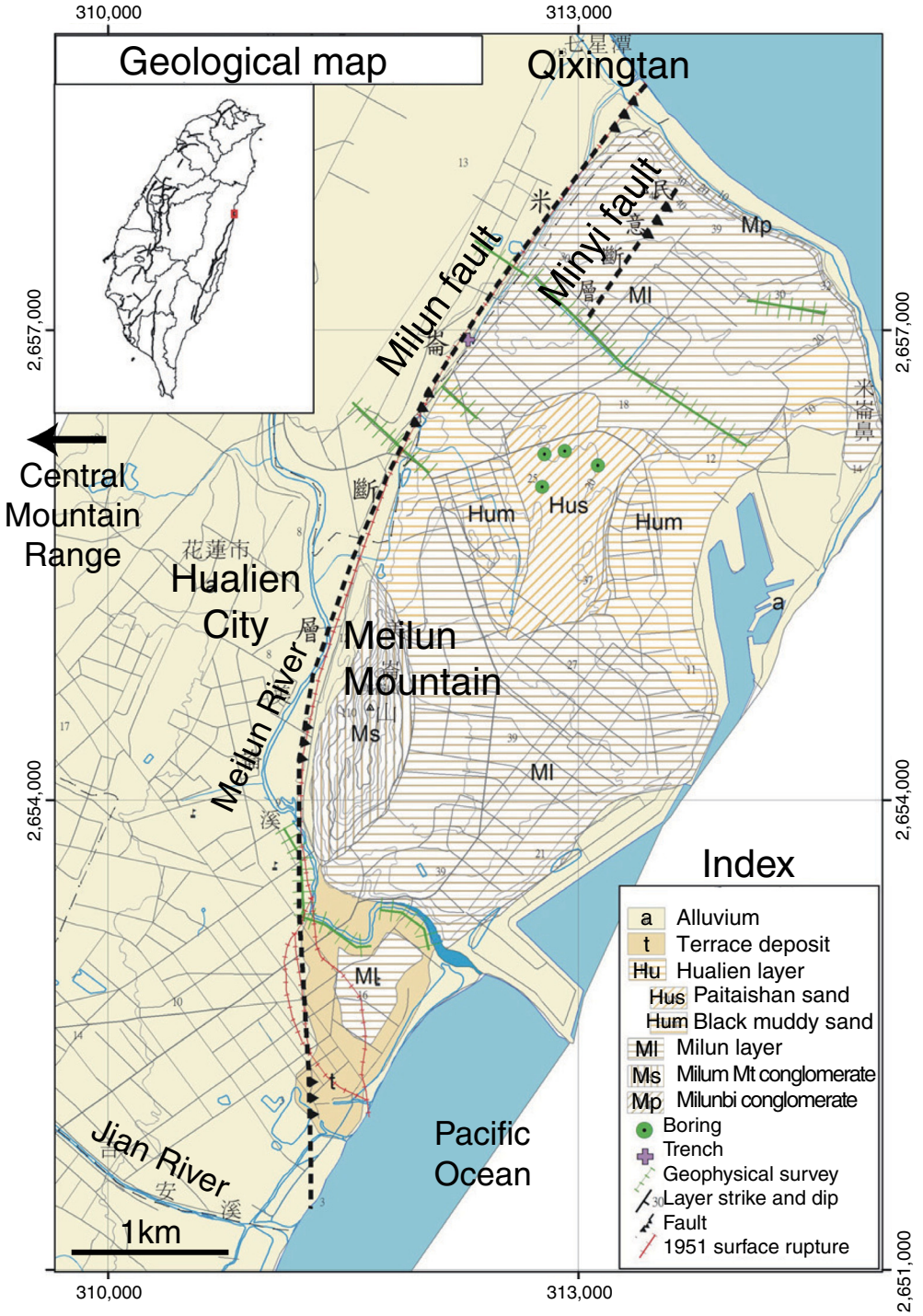

Figure 1. Geological map of the Hualien (modified after the geological map provided by Central Geological Survey, Taiwan; see Data and Resources). The coordinate system is TWD67 TM2. The inset is the map of Taiwan with the region of the geological in red square. The color version of this figure is available only in the electronic edition.

Hualien (Huang *et al.*, 2019) from the Qixingtan coast, through the west side of Meilun Mountain, to the old port (see Data and Resources). This fault was likely reactivated during the 2018 Hualien earthquake (Huang *et al.*, 2019; Lin *et al.*, 2019; Wu, Yen, *et al.*, 2019). Source models suggest that the fault dips to the east, and the slip is thrust movement with a left-lateral component (Kuo-Chen *et al.*, 2019; Lee *et al.*, 2019; Lo *et al.*, 2019).

There was an unusual pattern in the damage of the high-rise buildings. In Hualien city, four buildings totally collapsed with story failure, and one totally collapsed without story failure. All of these structures were located very close to the Milun fault based on the Reconnaissance report by the National Center for Research on Earthquake Engineering (see Data and Resources). Researchers have debated the relationship between the observed damage distribution and the fault rupture (e.g., Huang *et al.*, 2019; Lin *et al.*, 2019).

Ground motions at a site are influenced by the source, travel path, and local site characteristics. One possible explanation is that the building damage resulted from ground-motion amplification due to local soil structure. In this study, we performed microtremor measurements to investigate the shallow subsurface soil structure in the Hualien basin. We set a measurement line along a northwest–southeast section of the Hualien basin across the fault to see the difference in the shallow velocity structure. We also made measurements in the heavily damaged area where three high-rise buildings collapsed. Based on the inverted subsurface velocity structure, we will discuss the relationship between the subsurface soil structure and building damage.

STRONG MOTION AND BUILDING DAMAGE

The strong motions during the 2018 Hualien earthquake were recorded by the dense seismic networks of the Central Weather Bureau in Taiwan (Shin *et al.*, 2013) and the P-Alert

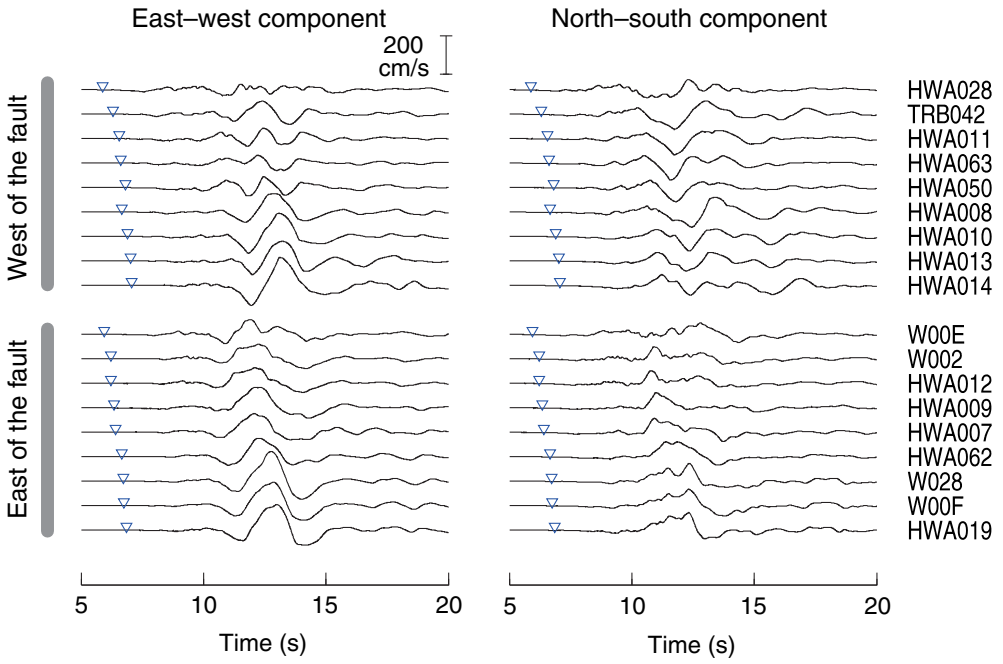

Figure 2. Velocity waveforms on the west and east sides of the fault from north to south. Inverted triangles show the theoretical *S*-wave arrival time. The horizontal axis shows the time after the origin time. The color version of this figure is available only in the electronic edition.

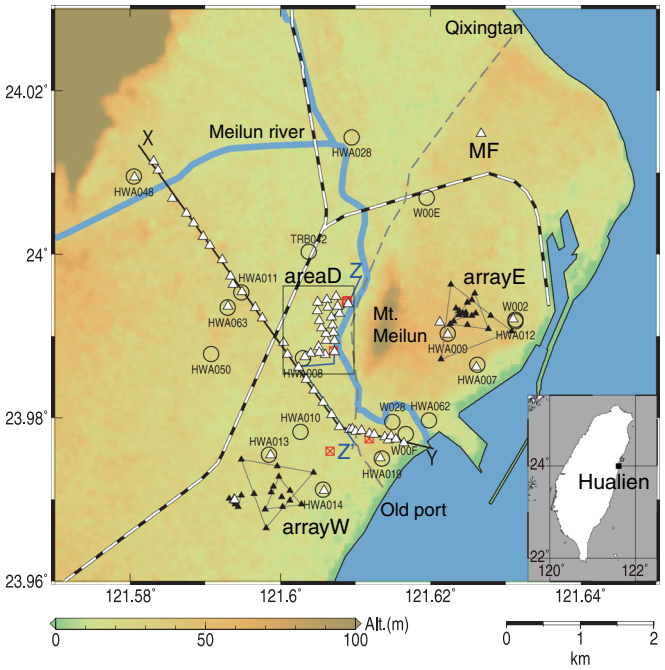

Figure 3. Map of the measurement locations. Open triangles show the locations of small arrays, and solid triangles show the locations of large arrays (array E and array W). Open circles show the locations of strong-motion stations. Square symbols with a cross inside show the location of the heavily damaged buildings. Background color shows the altitude. The broken gray line shows the location of the Milun fault (Huang and Huang, 2018). The railway is shown by a black and white line. The inset is the map of Taiwan with the location of Hualien. The color version of this figure is available only in the electronic edition.

Strong-Motion Network (Wu, Mittal, *et al.*, 2019). Downtown Hualien is located in a narrow basin (width of several kilometers) between the Central Mountain Range and the Pacific Ocean (Fig. 1). The Milun fault runs in a north–south direction through the center of the Hualien basin. The geology of the west side of the Milun fault is alluvium, and east side of the fault consists of either conglomerate or sandy layer.

There are 20 stations in the Hualien basin, with average spacing of about 1 km. Figure 2 shows the velocity records at the strong-motion stations on the east and west sides of the fault from north to south. The locations of the seismic stations are shown in Figure 3. The main pulse has a period of 3 s, and the phases of the waveforms are rather different between the east and west sides of the fault for the north–south component. The arrival of this large pulse is about 5 s later than the *S*-wave arrival from the hypocenter, which suggests that the source of this pulse is away from the hypocenter.

The acceleration response spectra in Figure 4 show different spatial patterns, depending on the period. The distribution of the response spectra at 0.5 s is relatively homogeneous over the basin, and the stations on the western side of the basin (HWA048 and HWA028) show slightly higher values. This suggests that the western side of the basin consists of thinner deposits, which may amplify the shorter-period ground motion. On the other hand, the long-period ground motions, with periods of 2–3 s, were strongly amplified near the southern end of the Milun fault.

A damage survey of the high-rise buildings was carried out in the Hualien basin by Kuo *et al.* (2018). The definition of high-rise buildings in Taiwan is 10 or more floors. There are five buildings rated as damage rank 5, according to the damage scale of Hsiao *et al.* (1999), that is, complete destruction, but most of the high-rise buildings were undamaged or sustained minor damage (Kuo *et al.*, 2018). The locations of the heavily damaged buildings are shown in Figure 3. It is interesting that the heavily damaged buildings are all very close to the fault surface rupture, but not concentrated near the southern end of the Milun fault, where the large-peak ground velocity was recorded (around the station W028).

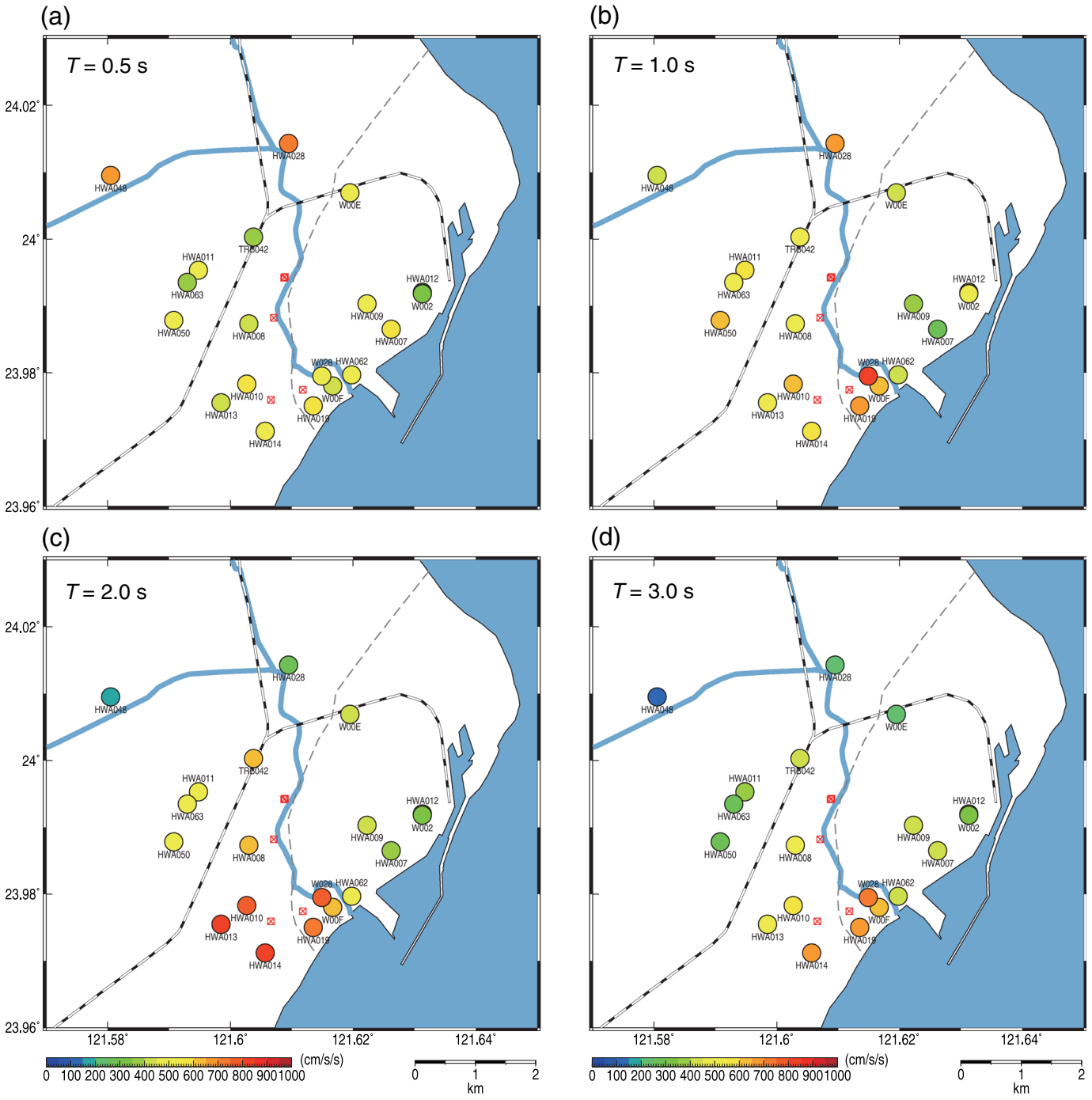

Figure 4. Acceleration response spectra for the east–west component during the mainshock at the period of (a) 0.5 s, (b) 1.0 s, (c) 2.0 s, and (d) 3.0 s. The damping is 5%. Other symbols are in the same format as in Figure 3. The color version of this figure is available only in the electronic edition.

MICROTREMOR SURVEY

We performed microtremor surveys in the Hualien basin from 20 to 26 October 2018. We used 10 seismometers (JU410) made by Hakusan Corporation to perform array measurements. The JU410 instrument includes three-component acceleration-type sensors, a logger, and a battery, in casing. The sampling frequency was set to 200 Hz, with the high-cut filter set at 80 Hz.

We performed small (scale of about 10 m) and large (scale of a few hundred meters) array measurements. The small array measurements were performed with five seismometers in arrays consisting of a regular triangle with a radius of 0.6 m, and two seismometers were set further apart along the line of the center of the triangle (see Fig. 5d). The distance of the two seismometers from the triangle is about 10 and 15 m. We performed these array measurements at 64 locations, as shown in

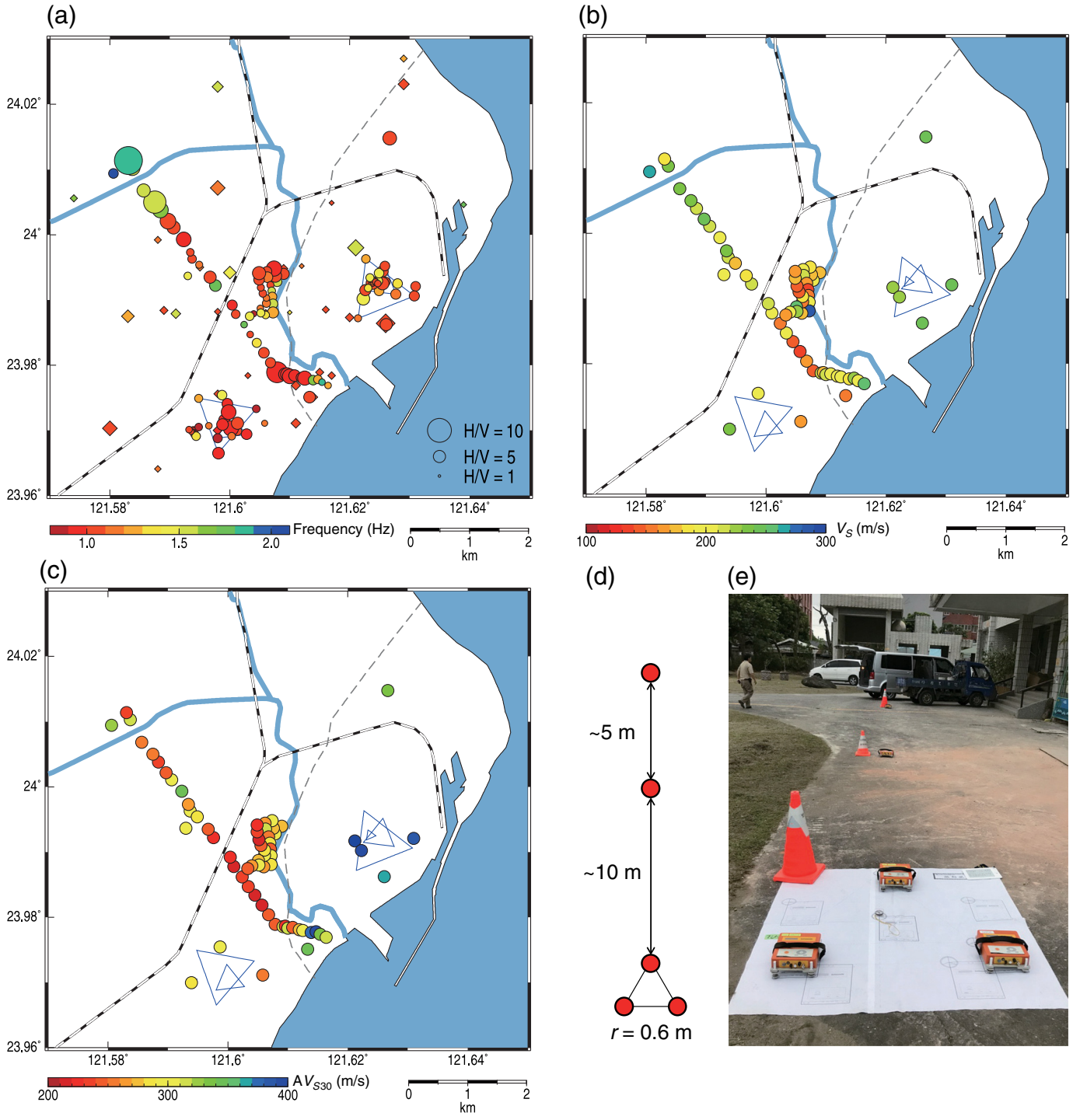

Figure 3. Locations of the small arrays were selected for three purposes. First, we measured along the line X–Y with a spacing of 50–200 m to obtain an east–west profile of the Hualien basin. We also performed 22 measurements within the heavily damaged area D in Figure 3 to evaluate the effect of subsurface soil structure on the building damage. For calibration, we performed measurements at the seven strong-motion stations (Kuo *et al.*, 2012) and the marble factory (Okamoto *et al.*, 1998) in which borehole logging data are available. We performed measurements for 15 min at each location.

Figure 5. (a) Peak amplitudes and frequencies of the horizontal-to-vertical (H/V) spectrum. The size and color of the symbols show the peak amplitude and peak frequency, respectively. Circles show the results of this study, and diamonds show the result of National Center for Research on Earthquake Engineering (NCREE) report (see Data and Resources). (b) *S*-wave velocity of the shallowest layer estimated from the phase-dispersion curve. (c) AV_{S30} directly estimated from the phase-velocity curves. (d) Sensor geometry for the small-array measurement. (e) Photo of the small-array measurement. The color version of this figure is available only in the electronic edition.

Large-array measurements were performed at two locations, on the east and west sides of the Milun fault (arrays E and W in Fig. 3). At each site, three different-size-array measurements (maximum radii of 100, 300, and 600 m) were performed. Each measurement was performed with seven seismometers; one at the center, three at the corners of a regular triangle, and three at the corners of the medial triangle. The array geometries are shown as solid triangles in Figure 3. The duration of the measurement is 45 min.

Small-array measurements were also performed at each center point of the large arrays to obtain subsurface velocity models for a wide depth range. In addition to this, medium-size-array measurements (radii of 9 and 17 m) were conducted using either regular or irregular triangle arrays with three seismometers, so that we can complementarily check the analysis results for both the small and large arrays.

The acceleration sensor in the instrument we used achieved a low noise level by optimizing the active element circuit (Tomioka and Yamamoto, 2006). According to the specification, the noise level is less than 0.1 (μ/G$\sqrt{Hz}$) at 1–30 Hz, and it was below this level at 0.5–40 Hz in the performance test (Tomioka and Yamamoto, 2006). We confirmed that the horizontal-to-vertical (H/V) spectrum obtained by our measurement showed a good agreement with that obtained by a broadband velocity sensor at the frequency 0.2–20 Hz (Kuo *et al.*, 2019) (Fig. S1, available in the supplemental material to this article).

METHOD

The obtained microtremor data were processed with the following methods.

H/V spectral ratios

The H/V spectral ratios (Nakamura, 1989) at each observation point were computed from the three-component microtremor waveforms. First, we split the time series into windows of 4096 points (20.48 s), with a 50% overlap; this resulted in approximately 50 windows for each measurement. This window length should be sufficient to capture low-frequency information for H/V in the range of 0.1–0.5 Hz. Before transforming the time windows into the frequency domain, a weighted Hanning window was applied. Windows with obvious transient noise were excluded from the analysis. A fast Fourier Transform (FFT) was applied to each individual time window to obtain the Fourier amplitude spectrum. Those spectra were then smoothed by a Konno–Ohmachi filter (Konno and Ohmachi, 1998), with a smoothing coefficient value $b = 20$. The horizontal component is defined as the geometric mean of the two components (electronic supplementary material of Bard, 2008). We visually checked that the peak frequencies of the two components were very similar. We used five seismometers at each observation point, and, consequently, we averaged the five H/V spectral ratios. We resampled the H/V curves with 64 logarithmically spaced samples between 0.25 and 10 Hz. These resampled curves were used as input to the inversion analysis.

Phase velocity

To obtain the Rayleigh-wave phase velocities, we applied the spatial autocorrelation (SPAC) method (Aki, 1957) to the vertical-component microtremor array data. In the determination of the phase velocities, power and cross-spectral densities were estimated with the techniques of both smoothing and ensemble averaging in the frequency domain (Bendat and Piersol, 2010). The waveforms of each small array were split into windows of 10.24 s duration, with 50% overlap; this resulted in approximately 100 windows per site, and a weighted Hanning window was applied. We apply an FFT to obtain magnitude-squared FFT spectra, which were then smoothed using a Parzen window with a bandwidth of 0.3 Hz. The smoothed spectra were averaged at each frequency (i.e., ensemble average).

A shorter window length was used to process the microtremor array data than for H/V spectral analysis, because the focus was on frequencies greater than a few hertz. It also enables stacking a large number of data segments, which contributes to improving the robustness. A phase-velocity dispersion curve may exhibit abrupt changes in frequencies higher than 10 Hz, at a site with thin sedimentary layers. Without a priori information on the local site condition, frequency-dependent windowing sometimes causes oversmoothing in high frequency. Therefore, we used the Parzen window, with a bandwidth of 0.3 Hz, to avoid oversmoothing at higher frequencies.

The calculated spectral densities were used to calculate the real part of the complex coherencies (SPAC coefficients). The obtained Rayleigh-wave phase velocities were resampled with logarithmically spaced samples between a few (1.1–3.0 Hz depending on sites) and 20 Hz, and used for the subsequent inversion analysis.

Joint inversion for the *S*-wave velocity structure

We inverted for the *S*-wave velocity (V_S) structure using the Rayleigh-wave phase velocities and H/V spectral ratios, following the method of Arai and Tokimatsu (2005). First, we constructed the initial model from the *PS* logging data at the surrounding strong-motion stations (see Data and Resources). The logging data at the stations west of the fault consist of three major layers: (1) very silty or clayey sand ($V_S \sim 200$ m/s), (2) silty gravels or well-graded gravels ($V_S \sim 300$ m/s), and (3) silty sand or silts with very fine sand ($V_S \sim 350$ m/s). We used these three layers for the top three layers of the initial model (Table 1). The logging data at the stations east of the fault include a silty gravel layer with higher velocity ($V_S \sim 600$ m/s) that we used as a fourth layer of the initial model.

We obtained a 1D velocity structure model at each observation point by iteratively improving the aforementioned initial model to explain the observed phase velocities and H/V spectral ratios. During the inversion procedure, the thickness

TABLE 1
Initial Velocity Structure for the Inversion

Layer Number	Thickness, ΔH (m)	Density, ρ (g/cm^3)	*P*-Wave Velocity V_P (m/s)	*S*-Wave Velocity V_S (m/s)
1	8	1.59	700	200
2	30	1.90	1400	300
3	30	2.02	1800	350
4	100	2.10	2100	600
5	—	2.17	2400	1000

and the *S*-wave velocity in each layer were set to be unknown parameters. The density was estimated based on the empirical relationship with the *P*-wave velocity (V_P) (Gardner *et al.*, 1974), and V_P was fixed at the initial model.

Because the observed H/V spectral ratios have multiple peaks, we considered single modes and multiple modes for both the Rayleigh and Love waves in the inversion procedure, in which the power partition ratios of Rayleigh to Love waves (R/L) were fixed to 0.7, as suggested by Arai and Tokimatsu (2005). Another approach to reducing the number of parameters is to use a fixed ratio of horizontal-to-vertical loading forces (HVLF; Parolai *et al.*, 2005; Picozzi *et al.*, 2005). Both the fixed R/L and the fixed HVLF are techniques for the simplification to compute the theoretical H/V spectra. We used a fixed R/L, which was observed from the field data and stable over time (e.g., Arai and Tokimatsu, 2000). The weights on the H/V spectral ratio and the phase-velocity dispersion curve for the inversion were set to 0.2 and 0.8, respectively. The weight of the H/V spectral ratio is small, but adding them increases the resolution at depth. A search range for the *S*-wave velocity in each layer was limited to 20% from the initial model, whereas no constraint was imposed on the thickness. The analysis was done using an analysis code "TremorDataView" (Senna and Fujiwara, 2008).

At the large-array sites, following Foti *et al.* (2018), the maximum depths of investigation were assumed to be the maximum aperture of the arrays or less (i.e., several hundreds of meters). At the small-array sites, on the other hand, the maximum depths of investigation were assumed to be several tens of meters, or a few times larger than the maximum array aperture. This expectation is based on our experience that small arrays have better relative resolution as compared to large arrays. As well, a joint analysis of phase velocity and H/V spectral data seems more effective for smaller arrays from the perspective of extending the analysis to low-frequency ranges.

Analysis of large array data

It was difficult to construct a detailed initial model to the depths corresponding to the large array surveys, due to the lack of data constraining geologic and geotechnical parameters at depth. Therefore, the large array data were analyzed by a method similar to that for the small arrays with the following difference. The duration and number of data segments used for the ensemble average were 20.48 s and 92 or 40.96 s and 53, respectively, depending on the array size. The bandwidth of the Parzen window was set to 0.1 or 0.3 Hz. We selected these values to avoid oversmoothing of the spectra at the target frequency. The phase velocity in the low-frequency (<2 Hz) domain was obtained by reading zero-crossing points of the SPAC coefficients (Ekström *et al.*, 2009).

Unlike the small arrays that have relatively more information on the shallow structure, the information to the depths corresponding to the large array is limited. Therefore, we constructed an initial model empirically (Ballard Jr, 1964). The initial models (number of layers and V_S) are updated by an empirical Bayesian approach (Cho and Iwata, 2019) to better explain the phase-velocity dispersion curve. It enables flexible modeling of shallow-to-deep structure by automatically determining the number of layers based on the Bayes factor. We inverted only the *S*-wave velocities for multiple thin layers, with the thickness of each layer fixed to a specific value.

RESULTS

H/V spectral ratios

Figure 5a shows the peak frequencies and peak amplitudes of the H/V spectra. The results reflect the local heterogeneous velocity structure, on a macroscopic scale, with a higher frequency peak (about 2 Hz) on the western mountain side (e.g., around the station HWA048), and a lower-frequency peak (about 1 Hz) around the Meilun River delta. The east side of the Milun fault, which is close to the coast (e.g., around the station HWA009), is at a slightly higher altitude, and the peak frequency is higher than the river sediment area (e.g., around the station HWA019).

Figure 6a shows the H/V spectra for the east–west section along the *X*–*Y* line in Figure 3. The peak frequency is higher on the west side of the basin (at 121.58° about 2 Hz) and gradually decreases to the east (at 121.59° about 1 Hz). The spectra at the floodplain of the Meilun River (121.605°–121.61°) have a very large amplitude peak at a frequency of 1 Hz, and the amplitude at higher frequencies is very small (Fig. 5a). This may indicate a strong velocity contrast in the subsurface structure. The east side of the Milun fault shows relatively flat spectra (121.612°–121.615°).

Phase velocity

We obtained four phase-velocity dispersion curves from the different sensor spacings in the small-array measurement: a regular triangle with a radius of 0.6 m and pairs of sensors with the distances of about 5, 10, and 15 m. These curves were connected to obtain a single phase-velocity curve across the frequency range of our interest (i.e., a few to 20 Hz). An example of the phase-velocity curves at the station HWA011 is shown in Figure 7b.

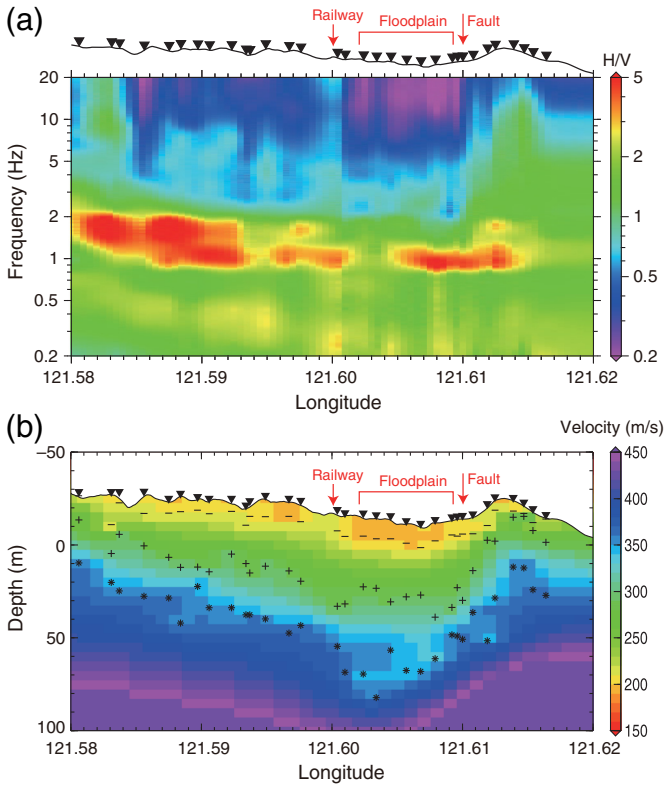

Figure 6. (a) H/V spectra along the *X*–*Y* section in Figure 3. Curves above the colored plots show the altitude, and triangles show the measurement location. (b) Inverted *S*-wave-velocity structure along the *X*–*Y* section in Figure 3. Bars, crosses, and asterisks show the velocity structure boundary for the first, second, and third layers, respectively. The color version of this figure is available only in the electronic edition.

Figure 5b shows the distribution of the minimum phase velocity of the dispersion curve, which generally corresponds to the *S*-wave velocity of the shallowest layer. The east side of the Milun fault and west of the railway clearly shows higher *S*-wave velocity at about 250 m/s. The *S*-wave velocity is lower on the west side of the Milun fault at about 150–200 m/s, probably due to the deposits of the Meilun River.

Figure 5c shows the distribution of the AV_{S30} determined by directly reading the Rayleigh-wave phase velocity, corresponding to the wavelength of 40 m. It is well known that the phase velocity at the wavelength of 40 m is a good approximation of AV_{S30} (Brown *et al.*, 2000; Konno and Kataoka, 2000; Martin and Diehl, 2004; Cho *et al.*, 2008; Albarello and Gargani, 2010). The figure indicates that AV_{S30} values east of the fault are greater than 300 m/s, whereas the values west of the fault are mostly smaller than 300 m/s.

Figure 8 shows the phase-velocity curves, including relatively low frequencies obtained from measurements of the large arrays on the east and west sides of the fault. The phase-velocity curves for the two sides of the fault are quite different in the frequency range at 1–10 Hz, indicating that the *S*-wave velocity of the shallow layers is greater on the east side of the fault compared to the west side of the fault. On the other hand, there may be little difference in the deeper structure.

Inverted velocity structure

We inverted for the velocity structure from the obtained phase-velocity curves. An example of the data fitting at the HWA011 station is shown in Figure 7. The black and gray curves show the observed and calculated data based on the optimal velocity structure, respectively. The fits for both H/V spectra, and phase-velocity curves are reasonably good. By inverting those two quantities simultaneously, we were able to obtain the velocity structure to the depth corresponding to the 1 Hz peak of H/V spectrum (about 50–75 m assuming V_S200–300 m/s). We visually checked the fit of all other sites and confirmed that the velocity models explained the observed data.

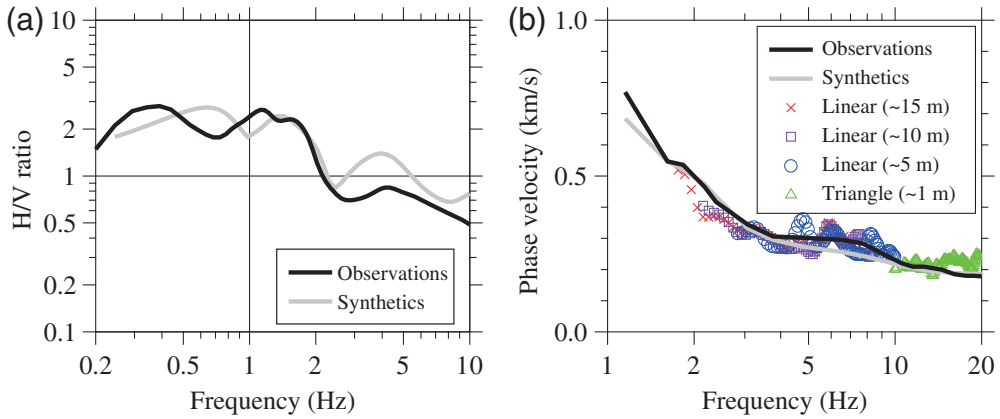

Figure 7. (a) Comparison between the observations (black) and synthetics (gray) for the H/V spectra. (b) Comparison of observed (black) and synthetic (gray) phase-velocity curves at the station HWA011. The individual curves for arrays with different sizes are also shown with symbols. The frequency ranges corresponding to the wavelength of 3–20 times of the array radius are shown. The color version of this figure is available only in the electronic edition.

Hualien basin profile. Figure 6b shows the velocity structure of the east–west section along the *X*–*Y* line in Figure 3. There is a large difference between the east and west sides of the Milun fault. The thickness of the first and second layers (V_S < 300 m/s) gradually increases from west to east, but suddenly decreases at the location of the fault. This change is much larger than the change of the topography at the ground surface. There is not a large difference in the thickness of the first layer,

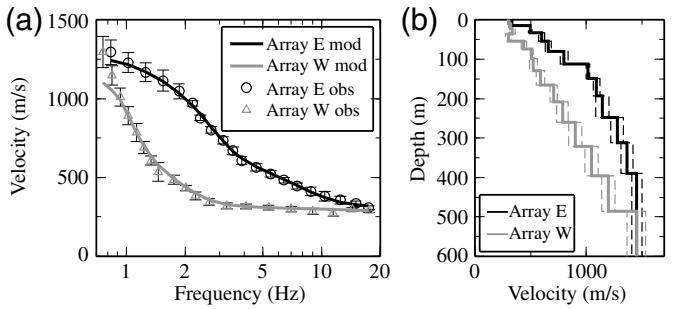

Figure 8. (a) Observed and estimated phase-velocity curves for the large array E (black) and array W (gray). Error bars for the observation are also shown. (b) Estimated velocity structure for the large array E (black) and array W (gray). Errors of the models are shown as thin-dashed lines.

but V_S is very low (<200 m/s) on the west side of the fault, which is assumed to be a floodplain of the Meilun River.

Deep structures. Figure 8b shows the inverted velocity structure for the phase-velocity curves obtained from the large array measurement. The *S*-wave velocity of the upper layers (depth < 500 m) is well resolved and greater on array E than on the array W. The greater V_S east of the fault is consistent with the Hualien basin profile shown in Figure 6b. The deeper structure (depth > 500 m) does not seem to have a large difference between the two arrays.

PS logging data at the strong-motion stations. To evaluate the accuracy of the velocity estimation, we compared the estimated velocity structure with the borehole *PS* logging data at the strong-motion stations (Fig. 9). We have seven stations with shallow-velocity profile logging data (about 30 m depth, see Data and Resources) and one station with deep logging data to 200 m (Okamoto *et al.*, 1998). Our results demonstrate good agreement between the obtained V_S depth profile and the available logging data, except for the HW019 station, in which logging data indicate V_S > 600 m/s at 15 m, whereas the inverted structure shows a V_S of only 350 m/s at the same depth.

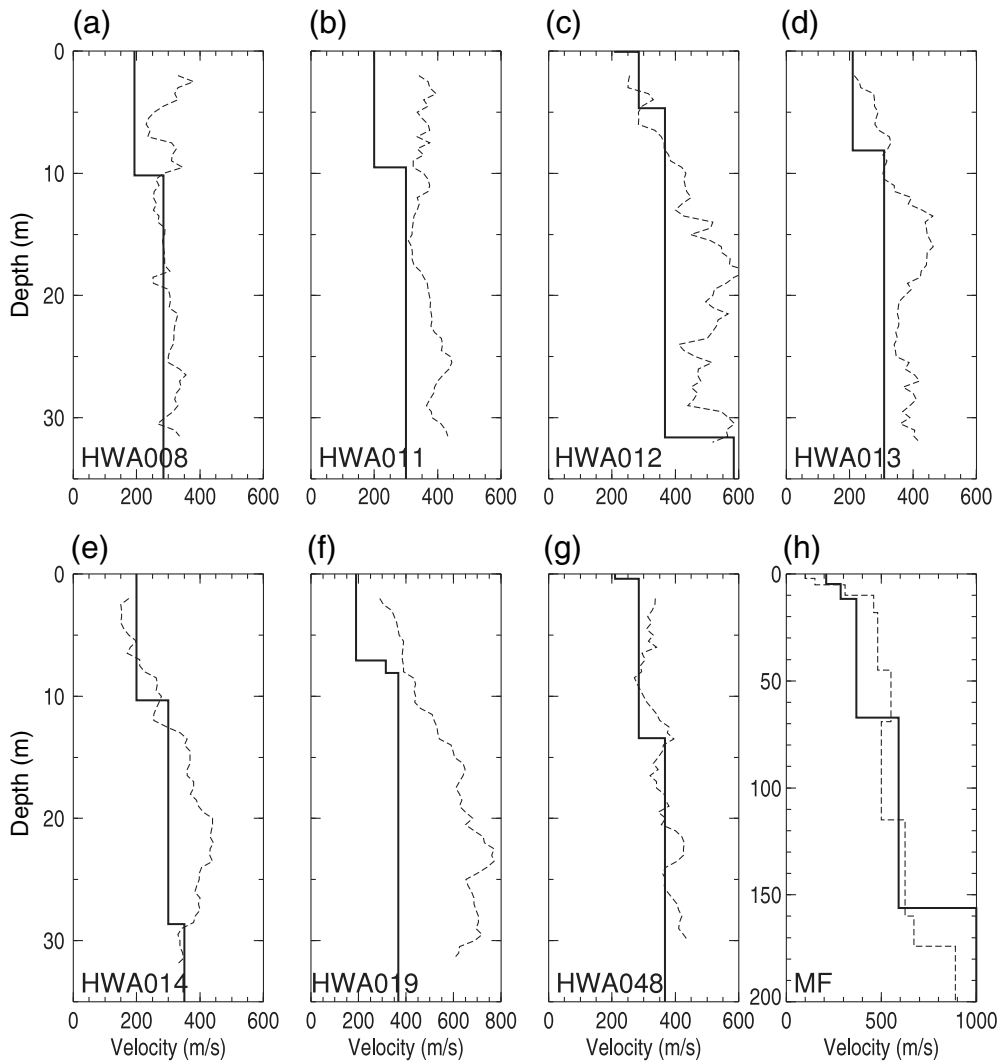

Figure 9. Velocity structures of the borehole logging data (dashed lines) and estimated velocity structures from the microtremor data (solid lines) at the strong-motion stations: (a) HWA008, (b) HWA011, (c) HWA012, (d) HWA013, (e) HWA014, (f) HWA019, (g) HWA048, and (h) marble factory (MF).

Phase-velocity curves estimated from the triangle and linear arrays. To verify the reliability of the linear array measurements, we compared phase-velocity curves obtained from the triangle and linear arrays at the site of the large array W, in which we have triangle arrays with radii of 0.6, 9, and 17 m and two-point linear arrays with distances of 5, 10, and 15 m. Figure 10a shows the phase-velocity curves estimated from these arrays. The phase-velocity curves estimated from the linear arrays are within ±20% of those estimated from triangle array results. At each site with a small array, we used a triangle

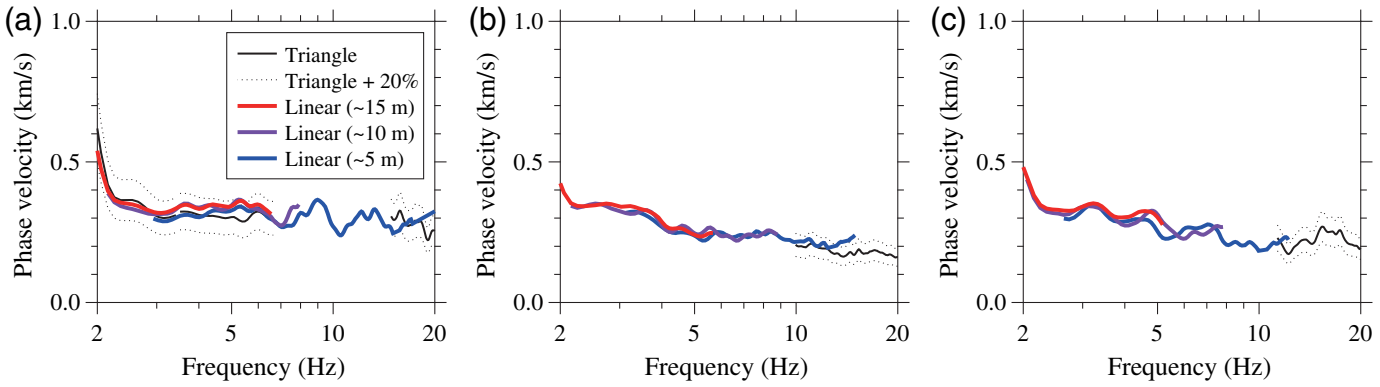

Figure 10. Observed phase-velocity curves for the (a) large array W, (b) HWA008, and (c) HWA014. Thick black lines show the phase-velocity curves estimated from the triangle array, and colored lines show those estimated from the linear array with two sensors. Broken lines show the range of ±20% from the estimation. The color version of this figure is available only in the electronic edition.

array, together with linear arrays, so that we can verify the reliability of the linear arrays at high frequency. For example, as demonstrated in Figure 10b,c, the results at the strong-motion stations show good agreement between the phase-velocity curves estimated from the linear and triangle arrays. These results suggest that the wavefield is close to "isotropic," in the sense that it is appropriate to use the SPAC method at these sites.

It is true that an isotropic wavefield is preferable for the SPAC analysis, in particular, when we use a linear array with two sensors (two-point array). However, it does not mean that a completely isotropic field is needed to obtain the dispersion curve. A two-point array has larger error than a circular array, but it has the advantage of requiring less space and fewer sensors. Cho (2020) demonstrated that the error is critical, if the microtremor wavefield is oriented at a single direction perpendicular to the axis of a two-point array, but, the error becomes smaller, if the azimuthal spreading of the wavefield becomes wider. In the field, the assumption of a wavefield with azimuthal spreading is more realistic than assuming a wavefield oriented in a single direction. In fact, Cho (2020) analyzed 400 microtremor array measurements and revealed that most of the two-point arrays analyzed had an error of <20%. The phase-velocity curves in Figure 10 suggest that the effect of an anisotropic wavefield was relatively small in, at least, the frequency range of these arrays.

The two-point array may not be suitable for certain situations. For example, we cannot use the two-point array for a wavefield with strong directional components (e.g., vicinity of factories that produce strong seismic noise). The regular polygon array is always preferable, as long as there is enough space and equipment. When we cannot avoid using two-point arrays, we need to check the isotropy of the wavefield for the SPAC analysis.

DISCUSSION

Subsurface velocity structure and regional tectonics

The Hualien basin is associated with the collision of the Philippine Sea plate and Eurasian plate (Angelier, 1986; Yu *et al.*, 1997). The basin is long and narrow in the north–south direction. The east side of the Milun fault (Hualien tableland) has a higher altitude than the west side of the fault, and the Meilun River runs along the fault (Fig. 3).

Although there is a general deepening of the shallow structure from west to east, our results show a large difference in the opposite sense across the Milun fault. The section profile of the velocity structure close to the fault shows that the thickness of the shallow layer is greater on the west side of the fault than on the east side of the fault. The velocity at the depths of less than 150 m, estimated from the large array, is also consistent with this feature. The AV_{S30}, shown in Figure 5c, also has a strong contrast with lower values on the west side of the fault and velocities larger than 300 m/s on the east side of the fault.

This velocity difference on the two sides of the fault is consistent with dip-slip faulting due to the tectonic structure (Angelier, 1986; Shyu *et al.*, 2016). The Hualien tableland was uplifted during the mainshock (Huang and Huang, 2018; Lee *et al.*, 2019; Lo *et al.*, 2019). Such uplift might accumulate on the east side of the fault over numerous earthquakes, which results in the higher altitude. The west side of the fault becomes relatively lower, and sedimentary deposits form the low *S*-wave-velocity layers near the surface.

Figure 6b was estimated from the surface-wave data, and the heterogeneous structure in the horizontal direction is affected by the resolution depending on the wavelength. That is, because the deeper part of the figure was estimated by waves with longer wavelengths, it may have a limited resolution to capture the sharp change of the velocity structure in the horizontal direction.

Relationship to the pulse-like strong motions

There was a characteristic pattern in the strong-motion distribution in the Hualien basin. The velocity waveforms show a large pulse-like waveform with a period of 3 s (Fig. 2) and large

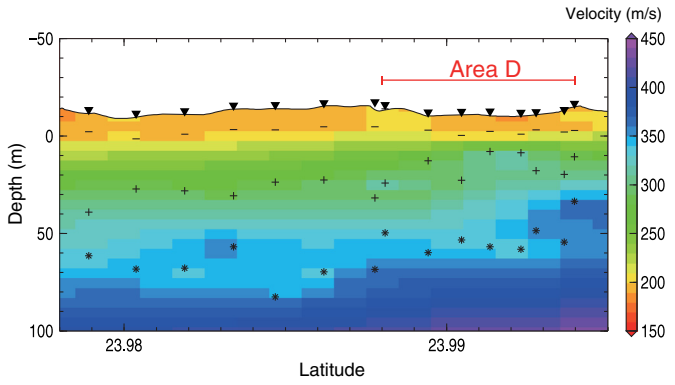

Figure 11. Inverted *S*-wave velocity structure along the Z–Z′ section in Figure 3. The symbols are in the same format as in Figure 6b. The color version of this figure is available only in the electronic edition.

amplitudes at the southern end of the Milun fault (Fig. 4d). This was observed on both the eastern and western sides of the fault. Ground motions are influenced by the source, path, and site characteristics. One possible explanation is that the large velocity pulse with 3 s period was generated by the local site response.

The results of our survey show that there is no significant shallow subsurface difference at the southern end of the Milun fault in comparison to the northern end, which could explain the distribution of building damage in this region. Figure 11 shows the *S*-wave-velocity structure in the north–south direction along the Meilun River (along the Z–Z′ section in Fig. 3). The section shows a horizontally layered structure and no significant change along the Milun fault. This is consistent with the tectonic regime of the Hualien region. Because of the east–west compressional tectonics, there is a substantial change of velocity structure in the east–west direction (Fig. 6b), but little variation in the north–south direction (Fig. 11).

Based on our large-array measurements, V_S reached 750 m/s at a 100 m depth. Suppose the 3 s velocity pulse was the response of the local velocity structure, then we would need a strong velocity contrast with a thick, low-velocity deposit (e.g., 450 m thickness assuming V_S600 m/s). Figure S2 shows the transfer functions for the velocity structures estimated from the large-array measurements, based on the 1D elastic site response (Haskell, 1960). The predominant frequencies for the arrays E and W are about 0.8 and 0.5 Hz, respectively.

The peak period of the ground motion during the mainshock was 3 s, but our data showed that it was difficult to explain this period from the subsurface soil amplification at least for the linear response. Figure 2 shows that the pulse-like ground motions are commonly observed at most stations, but the phase seems to be different on the east and west sides of the fault. The displacement records after the integration of these data show the static offset at this time (Kuo *et al.*, 2019). Kuo *et al.* (2019) concluded that this pulse-like ground motion might have been caused by the asperity, forward directivity amplification, and radiation pattern rather than the local site effect. Other studies also explain this 3 s pulse by source effects, such as rupture directivity and near-field waveform from the shallow fault segment with a large slip (Miyakoshi *et al.*, 2019; Wen *et al.*, 2019; Lin, Kanamori, *et al.*, 2020). Therefore, although we cannot exclude the possibility of the nonlinear response of the subsurface soil structure or 3D basin effects (Kawase, 1996), our results suggest that the 3 s velocity pulse was more likely generated by a source effect, rather than the local site response.

Relationship to the building damage

There were five buildings that were completely destroyed during the mainshock, and all of them were located very close to the fault surface rupture. It might be expected that the large velocities with 3 s period at the southern end of the Milun fault might be responsible for the damage to high-rise buildings, but the spatial pattern of long-period ground motions does not match the overall distribution of collapsed buildings (Fig. 4d). We focused on the heavily damaged area D in Figure 3, where three buildings collapsed and performed dense microtremor measurements to investigate the possible effect of local site characteristics on the damage of the structures.

Kuo *et al.* (2018) performed a damage survey for the high-rise buildings with 10 or more stories in that area. As shown in Figure 12, the buildings close to the river have more severe damage. Therefore, there is a debate on whether the reason for the collapsed buildings is the subsurface amplification due to the deposits of the river. The AV_{S30} distribution obtained from our survey showed slightly higher values close to the river (Fig. 12). This suggests that the shallow layers close to the river are unexpectedly hard compared to those farther from the river. This is probably due to the dip-slip faulting, as we have seen in Figure 6b. The first and second layers with low V_S have become thinner on the east side compared to the west side of the fault, because of the vertical deformation.

The natural period of the reinforced concrete structure can be approximated by 0.07 N (in which N is the number of the floors) (Hong and Hwang, 2000). We also performed microtremor measurements at the two 13-floor buildings, and their natural periods were 0.5 and 0.9 s, respectively. Wang *et al.* (2018) also estimated the natural period of high-rise buildings as 0.34–0.65 s from their microtremor survey. The design spectra for these periods are much higher than observed ground motions (Wang *et al.*, 2018). Therefore, high-rise buildings that satisfy the building code should not be seriously damaged by the ground motion corresponding to the linear site response (about 1 Hz). On the other hand, the ground motions at the period 2–3 s are extremely large and exceed the design level.

There are several possibilities for the cause of the collapse of the buildings, such as construction deficiencies (e.g., antiquate building codes, soft story, and rooftop additions indicated by Lin, Kuo, *et al.*, 2020), static offset at the fault, and near-source ground motion. If buildings do not have enough seismic

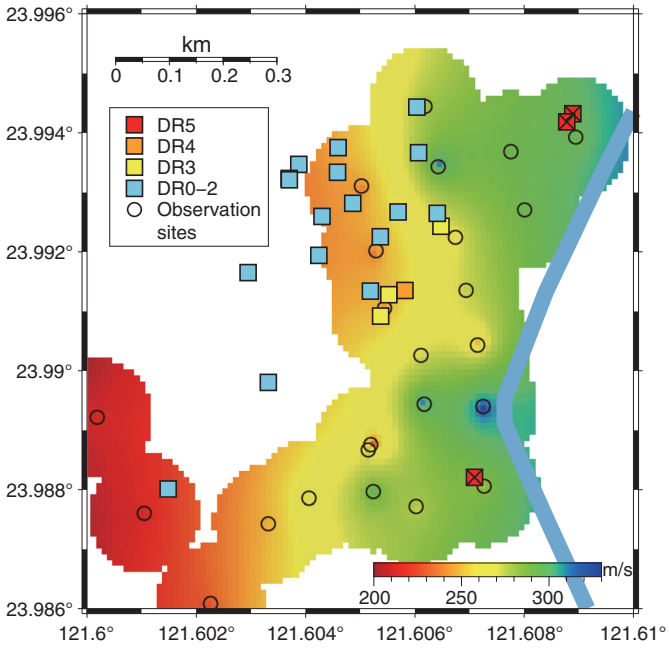

Figure 12. AV_{S30} (background color) and damage rank (square symbols) of the high-rise buildings in the heavily damaged area D. Open circles show the microtremor observation points. The thick line shows the Meilun River. The color version of this figure is available only in the electronic edition.

capacity, damage caused by a moderate shaking can cause severe degradation, which significantly increases the natural period of the building during the shaking. To understand the cause of building collapse, the site-specific ground-motion estimation and structure response analysis are necessary. However, from our field survey, the linear site response was dominant near 1 Hz, which did not explain the large pulse exceeding the design level.

CONCLUSION

We performed microtremor measurements in the Hualien basin, to investigate the shallow subsurface soil structure and evaluate their effects on the ground motion and building damage during 2018 Hualien earthquake. We have three major conclusions that may contribute to the clarification of the large velocity pulse and building damage.

1. Based on the inverted subsurface velocity structure, we found that the shallow subsurface structure deepens from west to east and then becomes shallower at the Milun fault. The shallowing across the fault is consistent with the faulting during the mainshock and the long-term tectonic displacement. Because of this offset structure across the fault, the AV_{S30} of the west side of the fault is generally smaller than that of the east side of the fault.
2. Our survey results show that there is no significant difference in the shallow structure at the southern end of the Milun fault, in which very large peak-to-peak velocity over 2 m/s was recorded. This large-amplitude 3 s pulse was probably generated by a source effect, rather than subsurface soil amplification.
3. As a result of the dense measurements in the damaged area, the locations where three buildings totally collapsed had relatively large AV_{S30} values, compared to the areas farther from the Meilun River. This suggests that the subsurface soil structure close to the river is unexpectedly harder compared to farther from the river. To clarify the cause of the collapse of these buildings, we need further investigations on the building construction and earthquake source characteristics.

DATA AND RESOURCES

We used the seismic waveform data recorded by the Central Weather Bureau (CWB) and the P-Alert Strong-Motion Network. The data can be obtained from the website at https://gdms.cwb.gov.tw/ and https://palert.earth.sinica.edu.tw/index_e.php. The moment tensor mechanism of the 2018 Hualien earthquake is available at the U.S. Geological Survey website (https://earthquake.usgs.gov/earthquakes/eventpage/us1000chhc/executive). The *PS* logging data at the strong-motion stations are available at Engineering Geological Database for Taiwan Strong Motion Instrumentation Program (TSMIP; http://egdt.ncree.org.tw/HWA_eng.htm). The fault map in Hualien was obtained from Hualien Prefecture Eastern Region Environmental Geology Research (http://geo.cpami.gov.tw/Case/97%E8%8A%B1%E8%93%AE%E7%B8%A3%E8%8F%AF%E6%9D%B1%E5%9C%B0%E5%8D%80%E7%92%B0%E5%A2%83%E5%9C%B0%E8%B3%AA%E7%A0%94%E7%A9%B6.htm, in Chinese). The geology map in Hualien was obtained from the National Geological Data Warehouse (https://gis3.moeacgs.gov.tw/gwh/gsb97-1/sys8/t3/index1.cfm, this link is no longer available). Reconnaissance report of seismic damages provided by the National Center for Research on Earthquake Engineering (NCREE) (in Chinese) is available at https://www.ncree.org/EarthquakeInfo/20180206/NCREE-2018-005F%E5%8B%98%E7%81%BD%E5%A0%B1%E5%91%8A.pdf. We used an analysis code "TremorDataView" (Senna and Fujiwara, 2008) for the joint inversion of velocity structures. The code used to determine observed phase velocities was a modified bersion of the software BIDO, which was downloaded from https://staff.aist.go.jp/ikuo-chou/bidodl_en.html. Some plots were made using the Generic Mapping Tools version 4.5.7 (Wessel and Smith, 1991). All websites were last accessed February 2020. The supplemental material includes two figures that compare the horizontal-to-vertical (H/V) ratio recorded by two sensors and transfer functions for the velocity structures estimated from the large-array measurements.

ACKNOWLEDGMENTS

The authors thank the Central Weather Bureau (CWB) and the P-Alert Strong-Motion Network for providing seismic waveform data. The field survey was supported by the international research collaboration funding in Kyoto University and the National Taiwan University - Kyoto University (NTU-KU) faculty exchange program. The authors acknowledge Tatsuya Noguchi in Tottori University for the use of their instruments.

REFERENCES

Aki, K. (1957). Space and time spectra of stationary stochastic waves, with special reference to microtremors, *Bull. Earthq. Res. Inst. Univ. Tokyo* **35,** 415–456.

Albarello, D., and G. Gargani (2010). Providing NEHRP soil classification from the direct interpretation of effective Rayleigh-wave dispersion curves, *Bull. Seismol. Soc. Am.* **100,** no. 6, 3284–3294.

Angelier, J. (1986). Preface, *Tectonophysics*, **125,** no. 1, IX–X.

Arai, H., and K. Tokimatsu (2000). Effects of Rayleigh and Love waves on microtremor H/V spectra, *Proc. of the 12th World Conf. on Earthquake Engineering*, Auckland, New Zealand, 30 January–4 February 2000.

Arai, H., and K. Tokimatsu (2005). *S*-wave velocity profiling by joint inversion of microtremor dispersion curve and horizontal-to-vertical (H/V) spectrum, *Bull. Seismol. Soc. Am.* **95,** no. 5, 1766–1778.

Ballard, R. F., Jr. (1964). *Determination of Soil Shear Moduli at Depths by In-Situ Vibratory Techniques*, Army Engineer Waterways Experiment Station, Corps of Engineers, Vicksburg, Mississippi, Miscellaneous Paper Number 4-691.

Bard, P. (2008). Foreword, *Bull. Earthq. Eng.* **6,** 1–2.

Bendat, J. S., and A. G. Piersol (2010). *Random Data: Analysis and Measurement Procedures*, John Wiley & Sons, Hoboken, New Jersey.

Brown, L., J. G. Diehl, and R. L. Nigbor (2000). A simplified procedure to measure average shear-wave velocity to a depth of 30 meters (V_{S30}), *Proc. of 12th World Conf. on Earthquake Engineering*, Auckland, New Zealand, 30 January–4 February 2000.

Cho, I. (2020). Two-sensor microtremor SPAC method: Potential utility of imaginary spectrum components, *Geophys. J. Int.* **220,** no. 3, 1735–1747.

Cho, I., and T. Iwata (2019). A Bayesian approach to microtremor array methods for estimating shallow *S* wave velocity structures: Identifying structural singularities, *J. Geophys. Res.* **124,** no. 1, 527–553.

Cho, I., T. Tada, and Y. Shinozaki (2008). A new method of microtremor exploration using miniature seismic arrays: Quick estimation of average shear velocities of the shallow soil, *Butsuri-Tansa (Geophys. Explor.)* **61,** 457–468 (in Japanese with English abstract).

Ekström, G., G. A. Abers, and S. C. Webb (2009). Determination of surface-wave phase velocities across USArray from noise and Aki's spectral formulation, *Geophys. Res. Lett.* **36,** no. 18, 1–5.

Foti, S., F. Hollender, F. Garofalo, D. Albarello, M. Asten, P. Y. Bard, C. Comina, C. Cornou, B. Cox, G. Di Giulio *et al.* (2018). Guidelines for the good practice of surface wave analysis: A product of the InterPACIFIC project, *Bull. Earthq. Eng.* **16,** no. 6, 2367–2420.

Gardner, G., L. Gardner, and A. Gregory (1974). Formation velocity and density—The diagnostic basics for stratigraphic traps, *Geophysics* **39,** no. 6, 770–780.

Haskell, N. A. (1960). Crustal reflection of plane *SH* waves, *J. Geophys. Res.* **65,** no. 12, 4147–4150.

Hong, L., and W. Hwang (2000). Empirical formula for fundamental vibration periods of reinforced concrete buildings in Taiwan, *Earthq. Eng. Struct. Dynam.* **29,** no. 3, 327–337.

Hsiao, C. P., H. H. Yeh, M. S. Sheu, K. C. Tsai, and Y. Q. Ding (1999). General report on damage in Chi-Chi earthquake—Damage investigation for building structures, *NCREE Research Rept. (Number NCREE-99-054)*, National Center for Research on Earthquake Engineering, Taiwan.

Huang, M., and H. Huang (2018). The complexity of the 2018 M_w 6.4 Hualien earthquake in East Taiwan, *Geophys. Res. Lett.* **45,** no. 24, 13,249–13,257.

Huang, S.-Y., J.-Y. Yen, B.-L. Wu, I.-C. Yen, and R. Y. Chuang (2019). Investigating the Milun fault: The coseismic surface rupture zone of the 2018/02/06 M_L 6.2 Hualien earthquake, *Taiwan. Terr. Atmos. Ocean. Sci.* **30,** no. 3, 311–335.

Kawase, H. (1996). The cause of the damage belt in Kobe: "The basin-edge effect," constructive interference of the direct *S*-wave with the basin-induced diffracted/Rayleigh waves, *Seismol. Res. Lett.* **67,** no. 5, 25–34.

Konno, K., and S. Kataoka (2000). An estimating method for the average S-wave velocity of ground from the phase velocity of Rayleigh wave, *Trans. Japan Soc. Civ. Eng.* **2000,** no. 647, 415–423.

Konno, K., and T. Ohmachi (1998). Ground-motion characteristics estimated from spectral ratio between horizontal and vertical components of microtremor, *Bull. Seismol. Soc. Am.* **88,** no. 1, 228–241.

Kuo, C.-H., J.-Y. Huang, C.-M. Lin, T.-Y. Hsu, S.-H. Chao, and K.-L. Wen (2019). Strong ground motion and pulse-like velocity observations in the near-fault region of the 2018 M_w 6.4 Hualien, Taiwan earthquake, *Seismol. Res. Lett.* **90,** no. 1, 40–50.

Kuo, C.-H., K.-L. Wen, H.-H. Hsieh, C.-M. Lin, T.-M. Chang, and K.-W. Kuo (2012). Site classification and V_{S30} estimation of free-field TSMIP stations using the logging data of EGDT, *Eng. Geol.* **129,** 68–75.

Kuo, K., P. Hsieh, S. Xu, and S. Lin (2018). Preliminary analysis on damage of building structures and interior space in the 20180206 Hualien earthquake, *The 14th National Conf. on Structural Engineering*, Taichung, Taiwan, 6–8 November 2018, Paper Number 24002 (in Chinese).

Kuo-Chen, H., Z. Guan, W. Sun, P. Jhong, and D. Brown (2019). Aftershock sequence of the 2018 M_w 6.4 Hualien earthquake in eastern Taiwan from a dense seismic array data set, *Seismol. Res. Lett.* **90,** no. 1, 60–67.

Lee, S., T. Lin, T. Liu, and T. Wong (2019). Fault-to-fault jumping rupture of the 2018 M_w 6.4 Hualien earthquake in eastern Taiwan, *Seismol. Res. Lett.* **90,** no. 1, 30–39.

Lin, J.-L., C.-H. Kuo, Y.-W. Chang, S.-H. Chao, Y.-A. Li, W.-C. Shen, C.-H. Yu, C.-Y. Yang, F.-R. Lin, H.-H. Hung, *et al.* (2020). Reconnaissance and learning after the February 6, 2018, earthquake in Hualien, Taiwan. *Bull. Earthq. Eng.* **18,** 4725–4754.

Lin, Y.-S., R. Y. Chuang, J.-Y. Yen, Y.-C. Chen, Y.-T. Kuo, B.-L. Wu, S.-Y. Huang, and C.-J. Yang (2019). Mapping surface breakages of the 2018 Hualien earthquake by using UAS photogrammetry, *Terr. Atmos. Ocean. Sci.* **30,** no. 3, 351–366.

Lin, Y.-Y., H. Kanamori, Z. Zhan, K.-F. Ma, and T.-Y. Yeh (2020). Modeling of pulse-like velocity ground motion during the 2018 M_w 6.3 Hualien earthquake, Taiwan, *Geophys. J. Int.* **223,** no. 1, 348–365.

Lo, C.-L., E. T.-Y. Chang, and B. F. Chao (2012). Relocating the historical 1951 Hualien earthquake in eastern Taiwan based on tide gauge record, *Geophys. J. Int.* **192,** no. 2, 854–860.

Lo, Y.-C., H. Yue, J. Sun, L. Zhao, and M. Li (2019). The 2018 M_w 6.4 Hualien earthquake: Dynamic slip partitioning reveals the spatial transition from mountain building to subduction, *Earth Planet. Sci. Lett.* **524,** 115729.

Martin, A. J., and J. G. Diehl (2004). Practical experience using a simplified procedure to measure average shear-wave velocity to a depth of 30 meters (V_{S30}), *Proc. of 13th World Conf. on Earthquake Engineering*, Vancouver, Canada, 1–6 August 2004.

Miyakoshi, K., Y. Matsumoto, M. Yamada, J. Mori, I. Cho, T. Hayashida, C.-H. Kuo, C.-M. Lin, Y.-T. Yen, K.-C. Kuo, *et al.* (2019). Estimation of underground structures around source area of the 2018 Hualien earthquake (M_w 6.4) using microtremor array observations, *Proc. of the Fall Meeting of the Seismological Society of Japan*, Kyoto, Japan, 16–18 September 2019 (in Japanese).

Nakamura, Y. (1989). A method for dynamic characteristics estimation of subsurface using microtremor on the ground surface, *Q. Rep. Railway Tech. Res. Inst.* **30,** no. 1, 25–33.

Okamoto, T., T. Kokusho, K. Nishi, Y. Tanaka, K. Kudo, K. Suzuki, T. Kawai, Y. Sawada, T. Ueshima, T. Kataoka, *et al.* (1998). Large-scale seismic test research at Hualien site in Taiwan—Results of site investigation and characterization of foundation ground, *Central Research Institute of Electric Power Industry (CRIEPI) Research Rept. U97062*, Tokyo, Japan (in Japanese).

Parolai, S., M. Picozzi, S. M. Richwalski, and C. Milkereit (2005). Joint inversion of phase velocity dispersion and H/V ratio curves from seismic noise recordings using a genetic algorithm, considering higher modes, *Geophys. Res. Lett.* **32,** L01303, doi: 10.1029/2004GL021115.

Picozzi, M., S. Parolai, and S. M. Richwalski (2005). Joint inversion of H/V ratios and dispersion curves from seismic noise: Estimating the *S*-wave velocity of bedrock, *Geophys. Res. Lett.* **32,** L11308 , 1–4.

Senna, S., and H. Fujiwara (2008). Development of analyzing tools for microtremor survey observation data, Vol. 1, *Technical Note of the National Research Institute for Earth Science and Disaster Prevention*, Report No. 313, available at https://dil-opac.bosai.go.jp/publication/nied_tech_note/pdf/n313.pdf (last accessed September 2020).

Shin, T.-C., C.-H. Chang, H.-C. Pu, L. Hsiao-Wei, and P.-L. Leu (2013). The geophysical database management system in Taiwan, *Terr. Atmos. Ocean. Sci.* **24,** no. 1, 11.

Shyu, J. B. H., C.-F. Chen, and Y.-M. Wu (2016). Seismotectonic characteristics of the northernmost Longitudinal Valley, eastern Taiwan: Structural development of a vanishing suture, *Tectonophysics* **692,** 295–308.

Tomioka, T., and S. Yamamoto (2006). Development of low noise accelerometer (JA-40GA), *JAE Tech. Rep.* **29,** 122–129 (in Japanese).

Wang, X., H. Si, K. Koketsu, M. Nagano, and J. Dang (2018). Building damage, strong ground motion characteristics and indoor damage of high-rise buildings in 2018 Hualien earthquake, Taiwan, *Proc. of the 15th Japan Earthquake Engineering Symposium*, Sendai, Japan, 6–8 December 2018, PS1-01-38 (in Japanese).

Wen, Y.-Y., S. Wen, Y.-H. Lee, and K.-E. Ching (2019). The kinematic source analysis for 2018 M_w 6.4 Hualien, Taiwan earthquake, *Terr. Atmos. Ocean. Sci.* **30,** 1–11.

Wessel, P., and W. Smith (1991). Free software helps map and display data, *Eos Trans. AGU* **72,** no. 441, 445–446.

Wu, B.-L., J.-Y. Yen, S.-Y. Huang, Y.-T. Kuo, and W.-Y. Chang (2019). Surface deformation of 0206 Hualien earthquake revealed by the integrated network of RTK GPS, *Terr. Atmos. Ocean. Sci.* **30,** no. 3, 301–310.

Wu, Y.-M., H. Mittal, T.-C. Huang, B. M. Yang, J.-C. Jan, and S. K. Chen (2019). Performance of a low-cost earthquake early warning system (P-Alert) and shake map production during the 2018 M_w 6.4 Hualien, Taiwan, earthquake, *Seismol. Res. Lett.* **90,** no. 1, 19–29.

Yu, S.-B., H.-Y. Chen, and L.-C. Kuo (1997). Velocity field of GPS stations in the Taiwan area, *Tectonophysics* **274,** nos. 1/3, 41–59.

Manuscript received 7 February 2020
Published online 22 September 2020